Volume 17
Number 41
7 November 2025
Pages 23745-24368

Nanoscale

rsc.li/nanoscale

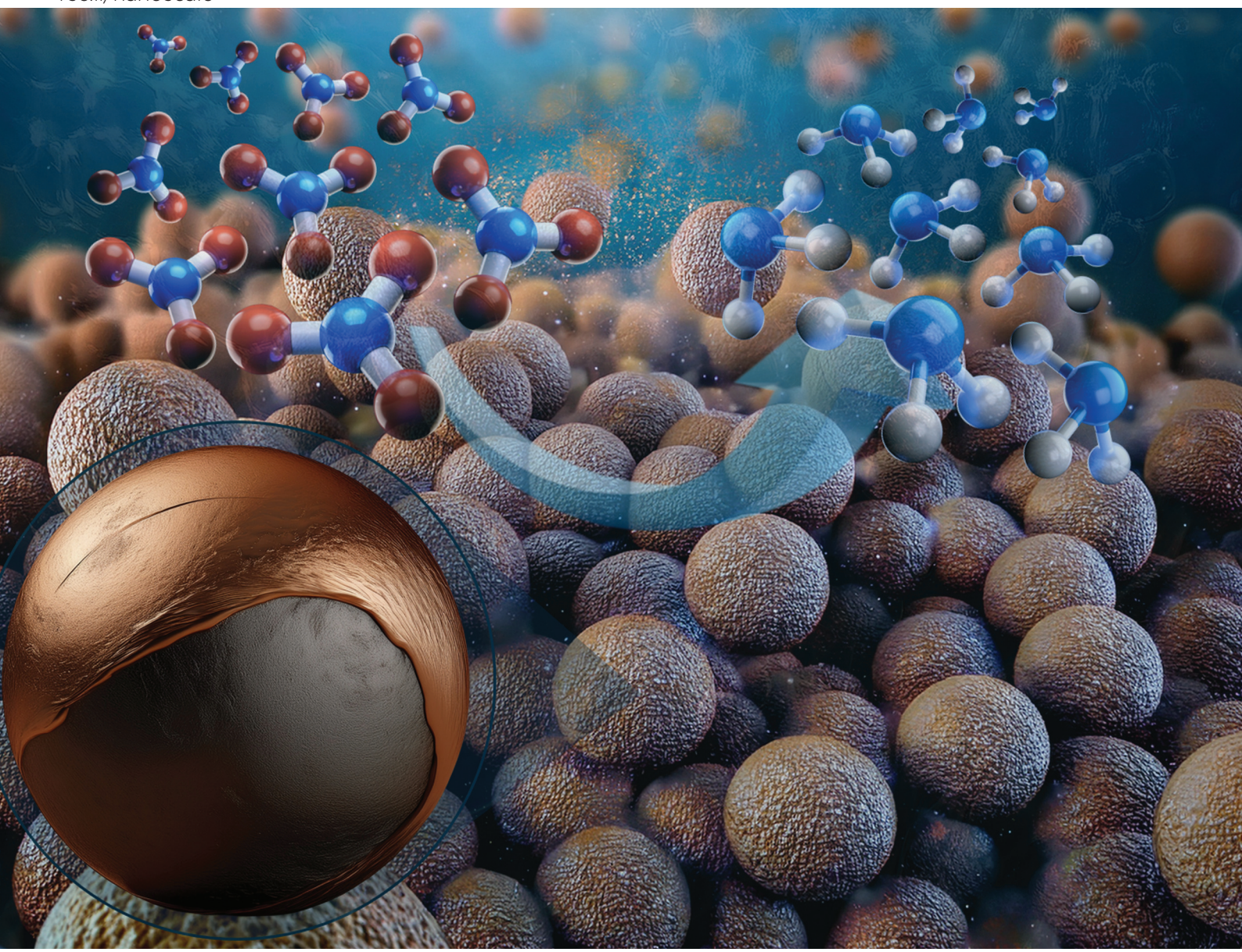

ISSN 2040-3372

ROYAL SOCIETY OF CHEMISTRY

PAPER
Robert Vajtai *et al.*
Core/shell BCN@Cu heterostructures *via* electroless deposition for interface-tailored electroactive materials

NCNST

Nanoscale

PAPER

View Article Online
View Journal | View Issue

Cite this: *Nanoscale*, 2025, **17**, 23948

Core/shell BCN@Cu heterostructures *via* electroless deposition for interface-tailored electroactive materials†

Arvin Taghizadeh Tabrizi,[a] Gergő Ballai,[a] Anastasiia Efremova,[a] Ákos Szamosvölgyi,[a] Dorina Gabriella Dobó,[b] Henrik Haspel,[a,c] Robert Vajtai *[d] and Zoltán Kónya[a,c]

Boron carbon nitrides (BCN) are semiconductors with tunable electronic band structures, and their heteropolar B and N bonding makes them suitable for electrochemical energy conversion applications. The latter is, however, restricted by poor control over phase formation as the properties of BCN strongly depend on the microstructure and the formed phases. A novel hybrid approach was utilized to control the BCN phase formation by combining mechanical alloying through ball milling and subsequent calcination at 400, 450, and 500 °C. In the next step, a thin layer of copper was deposited onto the BCN particles by electroless plating with and without prior surface activation using Pd^{2+} cations. Copper oxide was deposited on the as-prepared surface, whereas a core/shell Cu@BCN structure was formed by surface activation. The obtained heterostructures were tested in the direct electrochemical reduction of nitrate ions to ammonia (NO_3RR), a reaction of great promise for green ammonia synthesis in the future. Linear sweep voltammetry was carried out in a standard three-electrode electrochemical setup for alkaline NO_3RR at room temperature, and a current density of −19.2 mA cm^{-2} at −0.4 (V *vs.* RHE) and an ammonia faradaic efficiency (FE) and yield of 98.6% and 0.36 μg mg^{-1} s^{-1} were obtained after a 30 min electrolysis in 0.1 M KNO_3, respectively.

Received 31st May 2025,
Accepted 26th June 2025

DOI: 10.1039/d5nr02308d

rsc.li/nanoscale

1. Introduction

Boron-nitride (BN), and especially boron carbon nitride (BCN), materials attracted significant attention due to their tunable electronic and structural properties.[1,2] In the ternary system of B–C–N, phases with covalent bonding, such as diamond, graphite, B_4C, BN (both cubic and hexagonal), and g-C_3N_4, are notably stable. This stability facilitates the formation of BCN from these initial materials, with BC_4N and BC_2N being the most stable among the possible $B_xC_yN_z$ phases.[3] Generally, BCN is synthesized as thin layers or powders for catalytic applications across various fields. While BCN layers have been successfully formed *via* PECVD,[4,5] and ion beam assisted PLD,[6] synthesizing BCN in powder form remained challenging. A well-known issue is the poor reproducibility of BCN syntheses, which often result in varying properties and stoichiometry despite using identical methods.[1] Several synthetic routes exist for BCN production, each with limitations on purity and composition. The variability in reactivity and stability of BCN precursors during synthesis can lead to unwanted side reactions or impurities, impacting the quality of the final product.[7] Additionally, precursor availability and structural complexity pose further challenges in synthesizing high-quality BCN compounds. Thus, developing reliable synthesis methods using accessible precursors is crucial. A promising new route could be the transformation of B- and N-containing metal–organic frameworks (MOF) precursors, as the decomposition of MOFs results in high specific surface area doped carbon nanomaterials of various dimensionality,[8] even carbon nanotubes (CNT).[9]

Several complex and sophisticated methods exist for the fabrication of thin metal layers on various substrates, like chemical vapor deposition (CVD), physical vapor deposition (PVD), or atomic layer deposition (ALD).[10] Boron-nitride-based Cu/BN composites are well-known in the literature,[11] nevertheless BCN-supported systems were also prepared by thermal

[a]*Department of Applied and Environmental Chemistry, University of Szeged, Szeged, Hungary*
[b]*HUN-REN Reaction Kinetics and Surface Chemistry Research Group, University of Szeged, Szeged, Hungary*
[c]*Institute of Pharmaceutical Technology and Regulatory Affairs, University of Szeged, Szeged, Hungary*
[d]*Department of Materials Science and NanoEngineering, Rice University, Houston, TX, USA. E-mail: robert.vajtai@rice.edu*
† Electronic supplementary information (ESI) available. See DOI: https://doi.org/10.1039/d5nr02308d

condensation of copper nitrate to zerovalent Cu nanoparticle-decorated BCN[12] and Cu_2O/BCN[13] for dye degradation and photocatalytic hydrogen evolution, respectively. Electroless plating (ELP) or electroless metallization is the autocatalytic deposition of metals at the solid–liquid interface without using any external power source, *i.e.*, utilizing a redox reaction between the reducing agent in the plating bath and the metal ions being deposited onto the substrate. ELP was successfully used to deposit a wide range of metals, including copper.[14] Yet, no study has been found on the preparation of Cu/BCN *via* electroless plating, a cost-effective and simple method for fabricating Cu thin layer on BCN support.

Ammonia is one of the most essential industrial feedstocks traditionally produced by the energy- and carbon-intensive Haber–Bosch process.[15] The direct electrochemical reduction of nitrate or nitrite (NO_3RR) to ammonia is the technology of the future currently limited by low selectivity and yield,[16] while nitrate (NO_3^-) and nitrite (NO_2^-) ions, on the other hand, have a detrimental impact on the environment. NO_3RR is a promising route for mitigating the effect of nitrite and nitrate stress and the carbon footprint of ammonia synthesis at the same time.[17] Application of BCN compounds for electrocatalysis is scarce due to the generally low activity and poor synthesis reproducibility. The combination of BCN and an active co-catalyst can improve catalytic performance. For example, Kokulnathan *et al.* reported the synthesis of 3D flower-like nickel oxide particles entrapped in BCN as a catalyst for the electrochemical detection of nitrofurantoin,[18] and Li *et al.* embedded Pd nanocrystals in BC_2N for NO_3RR.[19] Further literature results identify Cu-based systems as potential catalysts,[20] like cerium-doped copper nanocrystals,[21] plasma-treated amorphous $MnCuO_x$,[22] Cu_2O/Cu grown on Cu foam,[23] Cu_2O nanocubes,[24] Cu distributed as single atoms in the BCN matrix with Pd nanoparticles (Pd_xCu/BCN),[25] or even 3D printed Cu electrode.[26] To our knowledge, a single report deals with copper-containing co-catalyst on BCN for nitrate reduction.[25]

Here, we developed a hybrid process combining mechanical alloying of simple and cost-effective precursors with calcination/pyrolysis for synthesizing boron carbon nitride. The as-prepared BCN was then used as a substrate for copper deposition to obtain a core/shell Cu/BCN structure *via* electroless plating with and without prior surface activation by Pd^{2+}. The formed phases were studied by X-ray diffraction (XRD), the chemical state of B, C, and N was determined by X-ray photoelectron spectroscopy (XPS), and the morphology was investigated by electron microscopy (TEM, SEM). The obtained Cu/BCN composite was tested in alkaline NO_3RR at room temperature.

2. Experimental methods

2.1. Materials

Boric acid (H_3BO_3), urea (CH_4N_2O), nitrogen gas, and melamine ($C_3H_6N_6$) served as the source of boron, nitrogen, and carbon, respectively. The copper electroless bath was prepared by using copper sulfate ($CuSO_4{\cdot}5H_2O$), potassium sodium tartrate ($KNaC_4H_4O_6{\cdot}4H_2O$), sodium hydroxide (NaOH), and formaldehyde (HCHO). $PdCl_2$ powders and HCl 30% were used for the surface activation treatment. All materials were used as received without any further purification steps.

2.2. Synthesis of boron carbon nitride (BCN)

In this procedure, a predetermined amount of melamine, urea, and boric acid at a ratio of 1 : 1 : 1 was poured into a Si_3N_4 container containing grinding balls of the same material. The ball-to-powder ratio was adjusted to 10 : 1, and ball milling was carried out at 450 rpm for 6 h. To obtain a homogenous milling and powder, a reverse rotation of the container once every 1 h was used. The obtained white powder was transferred to an alumina crucible and heated at 5 °C min^{-1} before being annealed at 400, 450, and 500 °C for 2 h under an argon atmosphere. After cooling down to room temperature, the resulting yellowish powders were grounded and labeled throughout the study as BCN-400, BCN-450, and BCN-500, respectively. Since challenges to BCN synthesis reproducibility are known in the literature, we synthesized more than 5 batches and verified their structure by comparing the corresponding XRD patterns to those achieved from the literature.

2.3. Synthesis of the Cu/BCN composite

The copper coating was applied on BCN *via* the electroless plating method. Prior to the electroless coating, surface activation was carried out, where 1 mg BCN was added to the solution of 0.75 g L^{-1} $PdCl_2$ in 15 mL L^{-1} HCl and stirred for 30 min. The activated BCN was settled out of the suspension, and the filtered and dried powder was subsequently introduced into the copper plating bath of 15 g L^{-1} $Cu_2SO_4{\cdot}5H_2O$, 3.3 g L^{-1} $NaH_2PO_4{\cdot}H_2O$ as a reducing agent, and 6 g L^{-1} $Na_2S_2O_3$ as stabilizing agent at 60 °C for 10 min. The pH of the solution was kept between pH = 11–13 with the addition of 1 M NaOH solution. After precipitation, the composite was filtered and dried at 60 °C for 24 h, and the sample was labeled as Cu@BCN. The color of the obtained heterostructures varied from black to reddish brown (copper color). To demonstrate the importance of surface activation in electroless metallization, copper plating of BCN was repeated without Pd^{2+} pretreatment (BCN-Cu_2O).

2.4. Structural characterization

Fourier-transform infrared (FT-IR, Bruker Vertex 70) was used to investigate the functional groups on the surface of the obtained samples in the 4500–450 cm^{-1} wavenumber region at 4 cm^{-1} resolution, averaging 16 spectra in each measurement. FT-IR samples were prepared by compressing the samples with potassium bromide (KBr) at a ratio of 1 : 100 and a pressure of 10 kN for 2 min. Pure KBr powders served as a reference. Differential scanning calorimetry (DSC) measurements (Mettler-Toledo DSC 3+) were performed to study the thermodynamic state of the raw materials used for BCN synthesis in

the temperature range of 25–600 °C at 2 °C min^{-1} heating rate. The DSC curves were evaluated using the STARe 9.30 software. X-ray diffractometry (XRD) was carried out on a Rigaku MiniFlex II desktop diffractometer with a CuKα source (λ = 0.1542 nm) operated at 30 kV and 15 mA to detect the phase formation between 2θ = 10–80° at a scan rate of 1 degree min^{-1}. The specific surface areas were calculated from N_2 adsorption–desorption measurements (Quantachrome NOVA 3000e) by the Brunauer–Emmett–Teller (BET) model. X-ray photoelectron spectroscopy (XPS) was performed to characterize the chemical state of the elements in as-prepared BCN and the composites. Spectra were recorded using a Specs XPS instrument equipped with a XR50 dual anode X-ray source and a Phoibos 150 hemispherical analyzer. The Al Kα X-ray source was operated at 150 W (14 kV). During measurement, sample charging was negated with an electron flood gun. Survey spectra were collected with 40 eV pass energy and 1 eV step size, whereas high-resolution spectra were measured with 20 eV pass energy and 0.1 eV step size. Samples were pressed onto double-sided carbon tapes attached to stainless steel sample holders. High-resolution spectra were background-corrected with a Shirley background, and peaks were fitted by a Gauss–Lorentzian product, where the Lorentzian contribution was 30%. The aliphatic component of the C 1s spectrum region at 284.8 eV was chosen as an inner reference. Scanning electron microscopy (SEM, Thermo Scientific Apreo C, 10 kV) and transmission electron microscopy (TEM, FEI Tecnai G^2 20 X-TWIN operated at 200 kV) were carried out to study the microstructure and morphology of the obtained samples. The surface charge and stability of the particles were characterized by the zeta potential of the samples, determined by dynamic light scattering (DLS) using a Malvern Zetasizer Nano ZS.

2.5. Electrochemical measurements

An Autolab PGSTAT302N electrochemical workstation connected to a standard three-electrode H-type electrolytic cell with a Nafion 115 exchange membrane separator was used for performing the electrochemical tests under alkaline conditions with (1 M KOH + 0.1 M KNO_3) and without (1 M KOH) the presence of nitrate ions. Platinum wire and calomel (Hg/Hg_2Cl_2 ALS/BASi) electrodes were used as the counter and reference electrodes, respectively. The working electrode was fabricated by electrophoretic deposition (EPD) of the BCN, Cu@BCN, and BCN-Cu_2O samples onto a 3 × 1 cm^2 carbon paper (QUINTECH) substrate. EPD was carried out between two pieces of carbon paper separated by 15 mm at 40 V for 30 min (electrolyte: 50 ml ethanol + 1 mg BCN), and the coated electrodes were dried at room temperature for 24 h. Before determining the electrochemical nitrate reduction activity, high-purity argon was bubbled for 30 min in the sealed cathode chamber. The potentials in this study are reported on the reversible hydrogen electrode scale (RHE), calculated from the raw data by the Nernst-equation R(RHE) = E(Ag/AgCl) + 0.0591·pH + 0.241 V. Afterwards, 5 cycles of cyclic voltammetry were carried out between −0.8 and 0.8 V (*vs.* RHE) at a scan rate of 100 mV s^{-1}, and immediately after that, a linear sweep voltammogram (LSV) was recorded from −0.5 to +0.2 V at a scan rate of 5 mV s^{-1}. The produced ammonia (in the form of NH_4^+) and the remaining nitrate (NO_3^-) were determined *via* UV-vis spectrophotometry colorimetric method using Nessler's reagents from a 50 µl aliquot diluted to 100× with distilled water.

3. Results and discussion

3.1. Synthesis of boron carbon nitride

The schematics of the synthesis of pure and copper-coated BCN is outlined in Fig. 1.

The XRD patterns of the $B_xC_yN_z$ formed at 400, 450, and 500 °C (BCN-400, BCN-450, and BCN-500) are shown in Fig. 2a. The amorphous state emerged during the high energy mechanical alloying, and the successful formation of the $B_xC_yN_z$ phase is confirmed by the reflections at $2\acute{I}$ = 26° and 43°, as these values correlate well with the peaks at $2\acute{I} \approx$ 26.2–26.4° found by Chen *et al.*,[27] Wang *et al.*,[28] and Mirzaee *et al.*[29] for BCN synthesized by calcination. The latter two studies reported an additional peak at $2\acute{I} \approx$ 45° at higher calcination temperatures, which matches the second diffuse reflection in Fig. 2a.

The formation of BCN through the reaction of the precursors urea, boric acid, and melamine was followed by calorimetry up to 600 °C. The DSC curve in Fig. 2b implies a three-step decomposition-transformation process during calcination. First, pre-melting and decomposition of urea occurred at

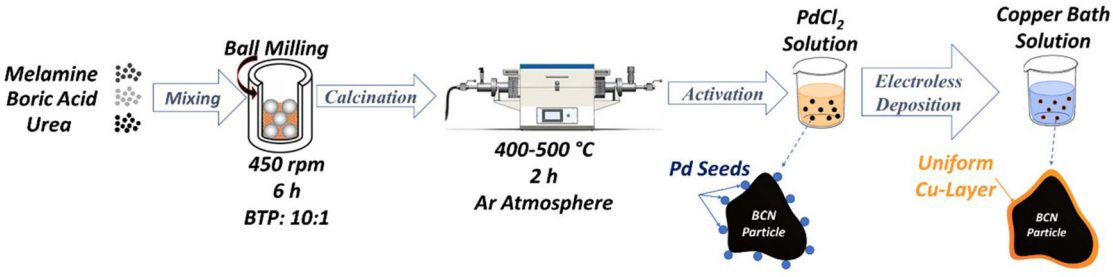

Fig. 1 Schematics of the synthesis of the Cu@BCN composite.

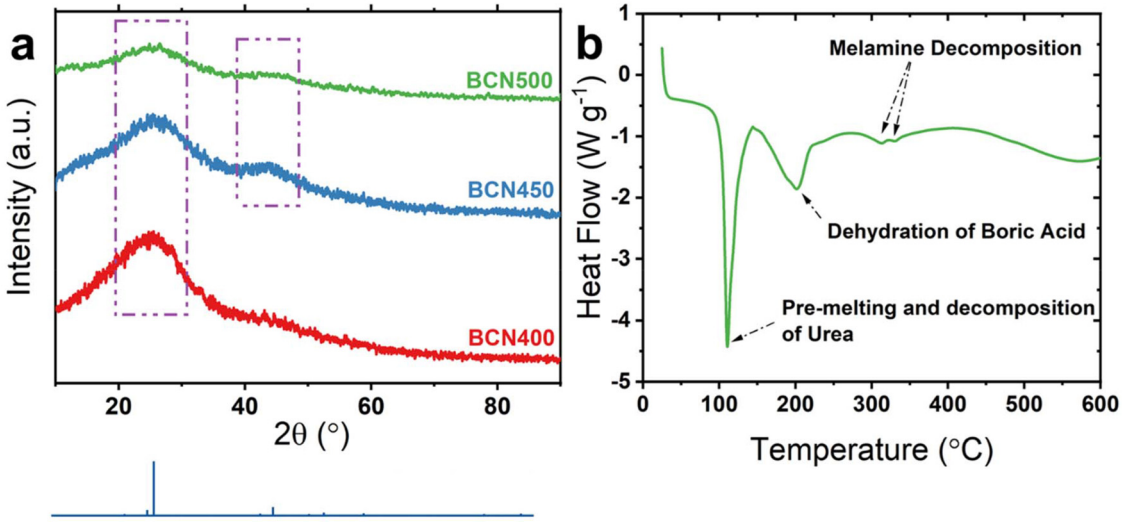

Fig. 2 XRD patterns of $B_xC_yN_z$ formed at 400, 450, and 500 °C along with the XRD pattern of BCN (a), and the calorimetric (DSC) curve recorded during the formation of $B_xC_yN_z$ from its precursors (b).

around 110 °C (eqn (1)) before boric acid dehydration and melamine decomposition took place at 203 °C (eqn (2)) and at approx. 331 °C (eqn (3)), respectively. The reaction of the products of eqn (1)–(3) then finalize the $B_xC_yN_z$ formation (eqn (4)), hence the choice of temperature region ≥ 400 °C in this study. A similar mechanism was previously proposed by Mirzaee *et al.* using glucose instead of melamine.[29]

$$CO(NH_2)_2 \rightarrow NH_3 + HCNO \quad (1)$$

$$3H_3BO_3 \rightarrow B_2O_3 + 3H_2O \quad (2)$$

$$C_3H_6N_6 \rightarrow NH_3 + H_3CN \quad (3)$$

$$B_2O_3 + 2NH_3 + xC \rightarrow 2BC_{x/2}N + 3H_2O \quad (4)$$

Table 1 Elemental composition of the $B_xC_yN_z$ samples from EDS measurements

Sample	B (at%)	C (at%)	N (at%)
BCN400	22.8	21.2	28.7
BCN450	23.9	18.7	32.5
BCN500	26.9	18.6	27.9

The elemental composition (atomic percent of boron, carbon, and nitrogen) was determined by EDS, and the results are presented in Table 1. The B : C : N ratio of 1.1 : 1 : 1.4, 1.3 : 1 : 1.7, and 1.5 : 1 : 1.5 was found for BCN400, BCN450, and BCN500, respectively. However, considering the different elemental sensitivities and ill-defined sampling volume, these ratios are only rough estimates. All we can see is that our B : C : N samples are close to that of the equiatomic composition; the obtained $B_xC_yN_z$ phases are located near the center of the B–C–N ternary phase diagram.

The morphology of the obtained BCN was studied by scanning electron microscopy, and the corresponding SEM images of BCN-400, BCN-450, and BCN-500 are presented in Fig. 3. All samples have large, agglomerated particles and flake-like morphology, which are tightly adhered to form bigger granular particles, similarly to those reported previously by Bhattacharyya *et al.*[30] The size of the macropores visible in the granular particles increases by increasing calcination temperature with an average pore size of around 10 μm in BCN500. The effect of the heat treatment temperature was studied by Zhang *et al.*, and they found ribbons-forming porous compact lamellar structures with a semi-flower morphology.[7] The origin of the porous structure can be attributed to the volatility (low

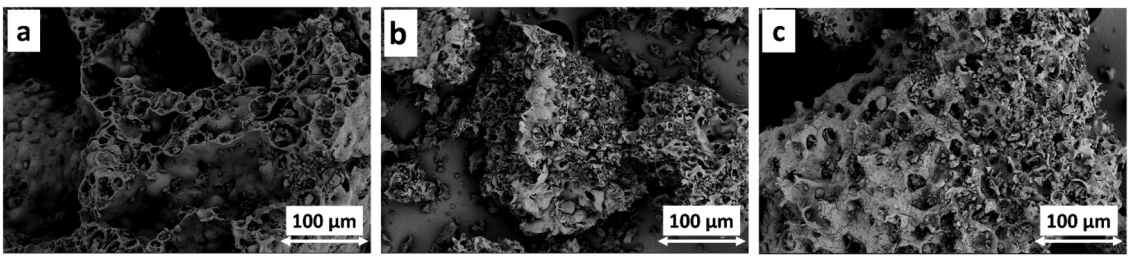

Fig. 3 Morphology of $B_xC_yN_z$ obtained at 400 °C (BCN400) (a), 450 °C (BCN450) (b), and 500 °C (BCN500) (c).

boiling point) of boric acid and was confirmed by DSC in Fig. 2b.[29]

The specific surface area of the samples was calculated from nitrogen adsorption isotherms using the BET model, and surface areas of 1.5, 1, and 20 $m^2\ g^{-1}$ were found for BCN400, BCN450, and BCN500, respectively. Regarding the precision of the specific surface area determination from adsorption–desorption isotherms *via* the BET method, we think that BCN400 and BCN450 have the same surface area within the experimental error while increasing annealing temperature results in an increased surface area. This is in agreement with the SEM images in Fig. 3, and shows the ability to obtain higher surface area BCNs by heat treatment for applications like sensors, catalysis, or energy storage. After optimization of the BCN synthesis, we chose the highest surface area BCN500 sample as a substrate for copper electroless plating and electrocatalytic applications.

3.2. Copper-coated BCN composite

We followed the change in morphology of BCN500 (Fig. 4a) upon copper plating without (Fig. 4b) and with Pd^{2+} surface activation (Fig. 4c). Without activation a non-homogeneous porous and compact structure was formed on the BCN500 substrate (Fig. 4b), whereas the deposited copper layer completely covered the BCN surface in Fig. 4c. In electroless deposition the redox reaction between Cu^{2+} and the reductant $H_2PO_2^+$ results in Cu layer formation, and the adsorbed Pd^{2+} on the particle surface provides seeds, *i.e.*, preferred sites for deposition. These nucleation sites accelerate the decomposition of the reductant in the bath, and due to the homogeneous coverage of metallic Pd crystallites on the substrate, more uniform metallic layers with good adherence can be grown.[31] Traditionally, surface sensitization by stannous chloride is done before the palladium autocatalytic center formation; however, anchoring Pd^{2+} *via* coordinative N–Pd σ bonds with the lone electron pair of nitrogen in the surface functional group can be achieved as well.[32] In our system the nitrogen-containing moieties of BCN likely serve as Pd^{2+} anchoring sites, which will be reduced to Pd by $H_2PO_2^+$. EDS results confirmed the high Cu content compared to the lower amounts of boron, carbon, and nitrogen.[33] Also, the obtained copper layer of Cu@BCN does not show any porous structure, which is consistent with the literature results.[34]

The TEM images in Fig. 4d–f illustrate the morphology and structure of the coated and uncoated BCN500, where the typical stacked 2D-lamellar structure of BCN can be seen as reported by Wei *et al.*[35] Fig. 4d demonstrates the irregular shape of the obtained BCN500 with wrinkles at the edges, an indication of the formation of folded ultrathin $B_xC_yN_z$ layers.[36] The amorphous structure of BCN500 found in the XRD patterns of Fig. 2a was further confirmed by SAED in Fig. S1,† where a diffuse diffraction pattern can be seen. Here, the diffraction ring corresponding to the (100) planes is visible, whereas that of the (002) planes is too close to the diffuse center to be evaluated. The outermost diffraction ring comes from planes of $d \approx 3.43$ Å, whose reflection can be found at $2\theta \approx 80°$ in the XRD patterns of BCN materials reported earlier.[27,28] The lack of presence of the latter peak in Fig. 2a is likely due to the somewhat higher amorphous nature of our system. In Fig. 4e, a copper coating on a BCN500 particle can be seen. This results of the inherent feature of electroless plating, where morphological complexity does not reduce surface accessibility, as electrophoretic (EPD) and electroless depositions (ELP) are capable of developing uniform layers on substrates of complex shapes. For instance, 5–10 nm Ni layers were deposited onto yttria-stabilized zirconia (YSZ) by EPD[37] and ELP with Pd^{2+} activation,[38] forming core–shell structures in both cases. Similar core–shell Cu@BCN can be seen in

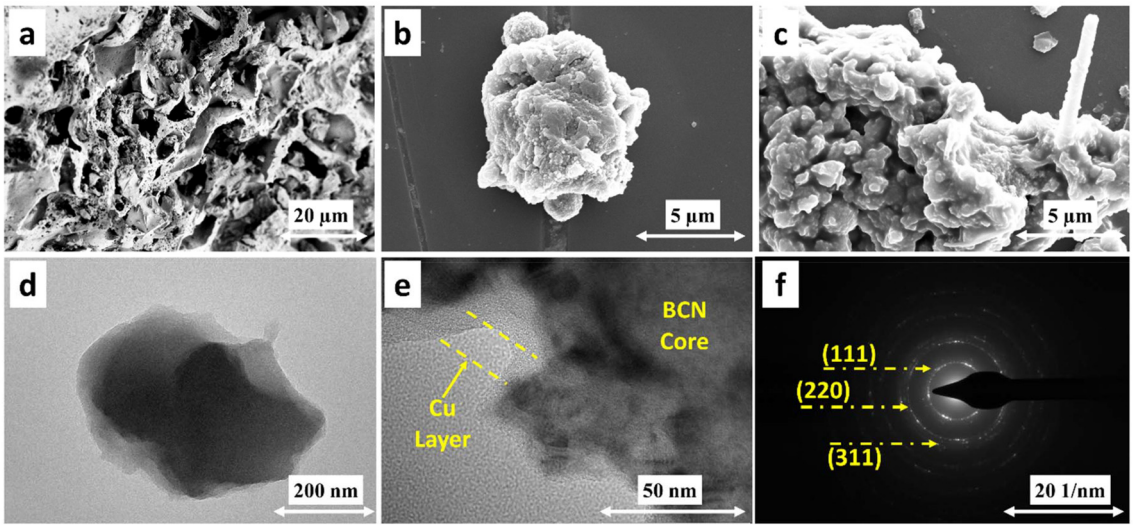

Fig. 4 Morphology change upon copper deposition followed by SEM: BCN500 (a), Cu_2O-BCN (b), Cu@BCN (c). TEM images of BCN500 (d), Cu@BCN (e), and the electron diffraction pattern of Cu@BCN (f).

Fig. 4e, where density variations through the actual grain is the result of the varying particle thickness. Neither copper particles in the thin boundary layer nor copper islands on the BCN particles were found, like in the electrochemically deposited Cu on nickel foam.[39] The electron diffraction pattern (SAED) of Cu@BCN in Fig. 4f corresponds to the (111), (220), and (311) planes of metallic copper. The XRD patterns of the copper-plated BCN500 with and without surface activation were compared to that of the as-prepared BCN500 in Fig. 5a. Peaks at $2\acute{I}$ = 43.5°, 50.6°, and 74.3° in the Cu@BCN pattern indicate the presence of a metallic copper layer in accordance with the SAED pattern of Fig. 4f above, whereas reflections at $2\acute{I}$ = 37.1°, 43.3°, 62.2°, and 74.5° correspond to the Cu_2O phase. This implies that without surface activation copper(I)-oxide layer is formed on the BCN500 surface instead of metallic copper deposition. Additionally, by applying copper layer on BCN500, the zeta potential of the particles changed from 8.3 mV of the as-synthesized BCN500 to −25.3 mV for Cu@BCN. Zeta potential (electrokinetic potential, ζ) is the electrostatic potential at the boundary layer separating the surface species and the dispersion medium relative to that of the bulk solvent, and $\zeta \approx \pm 30$ mV is considered a stable suspension.

The FT-IR spectra of the coated and uncoated BCN500 are shown in Fig. 5b. Based on the report by Liu *et al.*, the peaks at around 1375 and 810 cm^{-1} correspond to the B–N stretching and B–N–B bending vibration, respectively. The peaks between 1260–1330 cm^{-1}, 1020–1220 cm^{-1}, and 1090–1300 cm^{-1} indicate the presence of C–C, C–N, and C–B bonds, respectively, confirming the formation of the B–C–N bond.[40] In another study by Zhou *et al.*, the peaks at 1380 and 780 cm^{-1} attributed to the B–N and B–N–B bonds, respectively, and suggested the presence of the $B_xC_yN_z$.[41] Thus, vibration spectroscopy indicates the formation of B–C–N bonds in all samples obtained *via* our hybrid synthesis method. In addition, Chen *et al.* showed that the bands of O–H/N–H stretching at 3440 cm^{-1} and C–H stretching at 2925 and 2854 cm^{-1} can be related to the presence of the pristine $B_xC_yN_z$.[42] The IR spectrum of BCN500 changed upon copper and copper oxide deposition. However, the weak bands at 2934 and 2841 cm^{-1} were attributed to the CH_2 groups, including terminal groups of $-CH_3$ and $=CH$, which were previously detected for copper nanoparticles.[43] In Cu@BCN, peaks at 1609 and 1383 cm^{-1} likely originate from the asymmetric COO^- stretching related to carboxylate coordination to copper.[43] Also, applying a copper coating eliminated the peak of $B_xC_yN_z$ powders at 2188 cm^{-1}.

The XPS survey spectra for BCN500 and Cu@BCN are shown in Fig. 6, which confirms the successful deposition of the copper layer on BCN particles. The BNC500 sample contains only B, N, C, and O; no other impurity can be detected, as can be seen in Fig. 6a. The B 1s, C 1s, N 1s, and O 1s peaks are found at 187.3, 286, 398, and 530 eV, respectively. Upon applying a copper layer on $B_xC_yN_z$ powders, the intensity of the B 1s, C 1s, N 1s, and O 1s peaks decreases, which can be attributed to the copper coverage of BCN500. The high-resolution B 1s and N 1s spectra of Cu@BCN in Fig. 6b and c show the presence of B–C (191.1 eV), and both sp^2 (399.5 eV) and sp^3 (398.2 eV) C–N bonds in the BCN substrate, which further confirms the successful BCN synthesis *via* the hybrid method.[44] The high-resolution Cu 2p spectrum of Cu@BCN (Fig. 6d) in the 928–947 eV region was fitted with a multiplet splitting structure including Cu(0)/Cu(I), Cu(II)/oxide, and Cu(II)/hydrox-

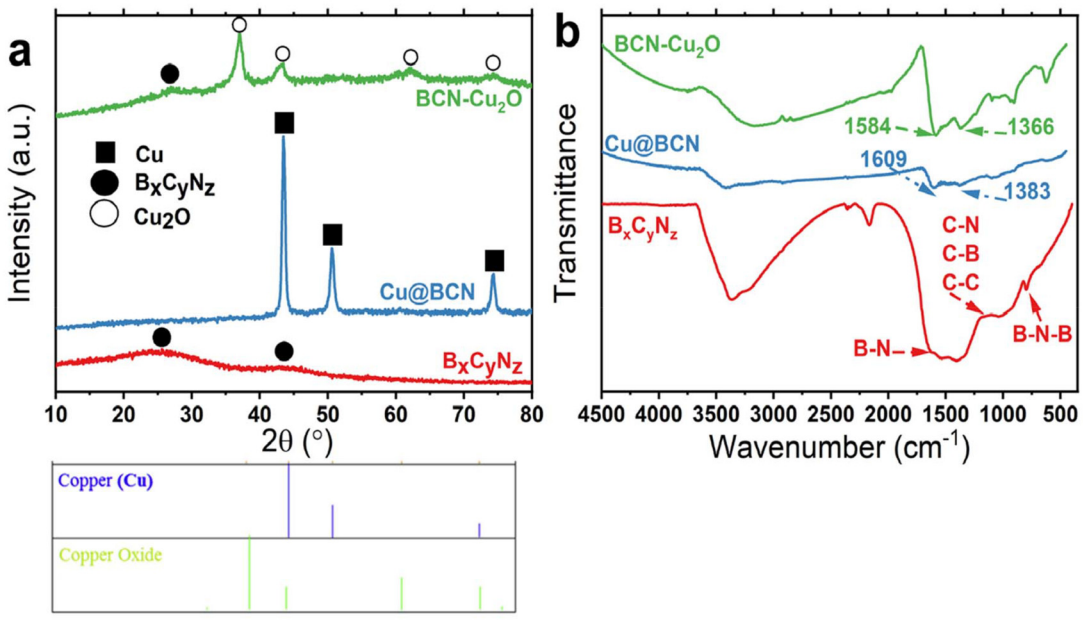

Fig. 5 XRD patterns (a), and FT-IR spectra (b) of the as-prepared BCN500, and the Cu/BCN composites prepared without (BCN-Cu_2O) and with surface activation (Cu@BCN). XRD patterns of copper and copper oxide are added for comparison.

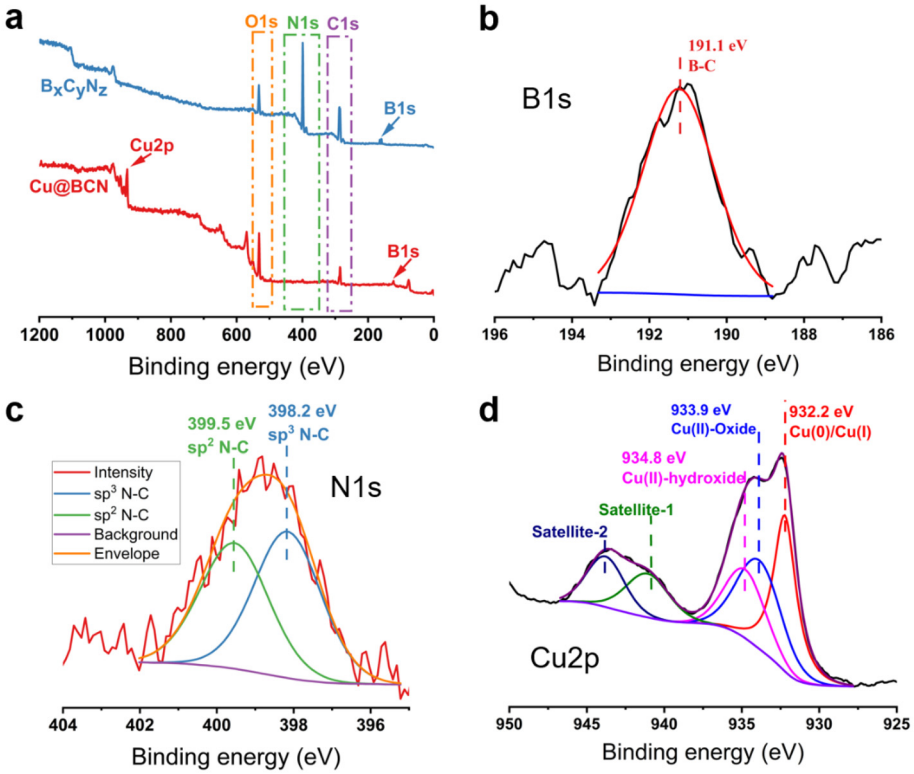

Fig. 6 XPS survey spectrum of BCN500 and Cu@BCN (a), and the high-resolution XPS spectra of B 1s (b), N 1s (c), and Cu 2p of Cu@BCN.

ide binding energy at 932.2, 933.9, and 934.8 eV, respectively. This is consistent with the results by Cerron-Calle *et al.*[45] The O 1s peaks can be originated from the adventitious carbon layer and the Cu compounds, while the intensity of the C 1s and N 1s peaks are almost identical in both samples, similarly to those reported by Lee *et al.* for boron and nitrogen co-doped graphene.[46] Detailed analysis of the high-resolution C 1s, O 1s, B 1s, and N 1s XPS spectra of BCN500 and the C 1s spectrum of Cu@BCN are depicted in Fig. S3.† Elemental composition of the two samples was calculated based on the peak areas corrected by the relative sensitivity factors based on Scofield cross-sections, and 5.2 at% of copper was found in the Cu@BCN composite (Table 2).

3.3. Electrochemical nitrate reduction

The NO_3RR activity of the Cu@BCN composite was evaluated by linear sweep voltammograms (LSV) recorded between −0.4 and 0.4 V (*vs.* RHE) under alkaline conditions in argon-purged 1 M KOH electrolyte at room temperature.[47] The obtained LSV curves with (NO_3RR) and without (HER) adding 0.1 M KNO_3 nitrate source to the electrolyte are presented in Fig. 7. It can be seen in Fig. 7a and b, that both samples, BCN500 and Cu@BCN, show some low water reduction activity (red lines), which increases in NO_3RR by the addition of nitrate ions (blue lines). However, the onset potential decreases upon copper deposition on BCN500 from −0.2 to −0.05 V (*vs.* RHE), reaching a current density of −4.74 and −19.20 mA cm^{-2} at −0.4 V (*vs.* RHE) for BCN500 and Cu@BCN, respectively. On Cu_2O-BCN, the onset potential was similar to that of BCN500 but with a steeper increase in current density towards more negative potentials, reaching a value of −5.69 mA cm^{-2} @ −0.4 V (*vs.* RHE) in Fig. 7c. Nitrate and water reduction (hydrogen evolution, HER) are competing processes, and even though the HER activity increased on Cu@BCN, the rise in the NO_3RR activity dominates the electrochemical behavior caused by the low activity and the hydrophobic feature of BN-based materials. CA experiments were carried out (Fig. S4†), and the amount of formed ammonia was determined by UV-vis spectroscopy (Fig. S5†). Yield rates were calculated *via* eqn (S2)† for BCN, Cu@BCN, and Cu_2O-BCN, and values of 0.73, 0.92, and 0.36 μg s^{-1} mg_{cat}^{-1} were obtained, respectively. Additionally, calculated FEs (according to eqn (S1)†) for BCN, Cu@BCN, and Cu_2O-BCN equal 96.5 98.9, and 98.6%, respectively.

In electrochemical nitrogen reduction reaction (N_2RR), the source of N for the formation of ammonia is often some N-species in the sample or solvent residue, as it has been evidenced several times after the rigorous protocol on the N_2-to-NH_3 reaction was published.[48] However, considering the

Table 2 Elemental composition of BCN500 and Cu@BCN from XPS measurements

Sample	B (at%)	N (at%)	C (at%)	O (at%)	Cu (at%)
BCN500	18.4	39.2	28.6	13.8	—
Cu@BCN	1.7	2.8	53.5	36.8	5.2

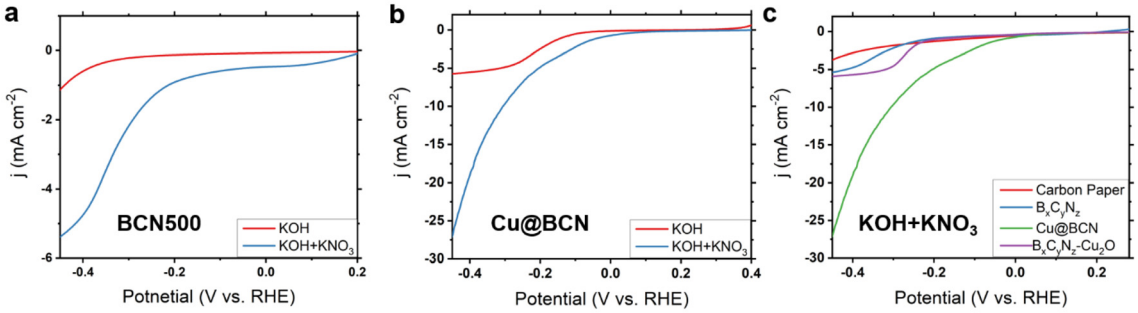

Fig. 7 Voltammetric (LSV) curves of BCN500 (a) and Cu@BCN (b) on carbon paper under alkaline conditions (1 M KOH) with and without the presence of nitrate ions (0.1 M KNO_3). Comparison of the NO_3RR activity of the bare carbon paper substrate, BCN500, and Cu@BCN in 1 M KOH + 0.1. KNO_3 electrolyte (c).

decomposition temperatures of urea (110 °C) and melamine (330 °C), it is unlikely that even a trace amount of the precursors remained in the product. If some ammonia was produced by the reduction of a trace amount of urea and melamine, we should see an elevated NO_3RR activity on pure BCN, whereas BCN was shown to be highly inactive in Fig. 7c. Moreover, it is worth noting that in N_2RR the interference of N-containing residue reduction is relevant due to the exceptionally low faradaic efficiency and yield. The amount of ammonia formed from this contamination could be comparable to that generated by the transformation of gaseous nitrogen reactant. In nitrate reduction, on the other hand, faradaic efficiency and ammonia yield are higher, and thus, the reduction of a trace amount of N-residue can simply be neglected. Furthermore, performing NO_3RR on isotope-labeled nitrate proved that ammonia is formed exclusively by the reduction of nitrate despite using an N-doped carbon framework-based Fe SAC catalyst.[49] Similar results were found on a Cu-based catalyst, as $^{15}NH_3$ originated solely from the transformation of isotope-labeled nitrate ions.[39]

The obtained current density on Cu@BCN is higher than the values reported for copper foils, copper nanocubes, and copper nanosheets by Fu *et al.*[50] and for a CuCo compound by Wang *et al.*[51] However, Zhao *et al.* obtained higher NO_3RR activity by distributed copper as single atoms in the B–C–N matrix with Pd nanoparticles ($Pd_{10}Cu$/BCN).[25] The charge transfer resistance of the carbon paper-based electrode was characterized by electrochemical impedance spectroscopy (EIS); the corresponding impedance spectra are seen in Fig. 8a. The diameter of the resulting semicircle in the Nyquist plot decreased in the BCN500–Cu_2O-BCN–Cu@BCN series, where the smallest semicircle of Cu@BCN implies the lowest charge transfer resistance among the samples.

Although there are no previous publications on Cu/BCN electrochemical nitrate reduction catalysts, a Cu-containing BCN-based system was studied in detail.[25] Here, Cu single atoms were dispersed into a BCN matrix with Pd nanoparticles (Pd_xCu/BCN). DFT calculations showed that copper is most probably in the form of Cu^{2+} in a CuN_4 configuration, where the lower Fermi level, *i.e.*, higher electron affinity, favors NO_3^-

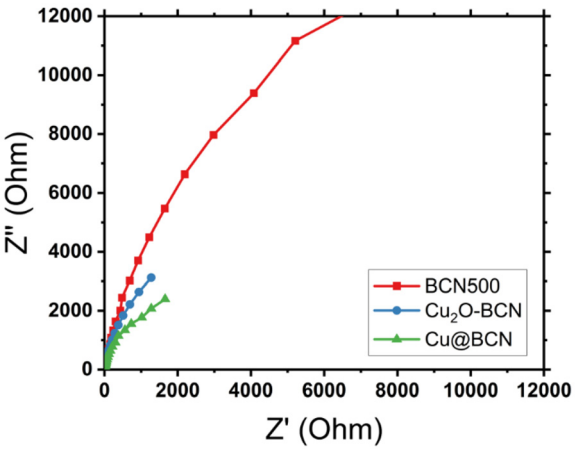

Fig. 8 Electrochemical impedance spectra (EIS) of BCN500, Cu_2O-BCN, and Cu@BCN deposited on carbon paper.

adsorption. It was also found that electrons are localized mainly on the B, C, and N atoms and delocalized on Cu and Pd. Calculations revealed electron transfer from BCN to Pd, but no electron transfer was observed between the two metal species. They found that BCN alone shows an order of magnitude lower NO_3RR activity compared to that of Pd_xCu/BCN. And even when BCN sites are available in $Cu(N_4)$/BCN, nitrate adsorption energy is positive on B, C or N, whereas it is negative on copper. Thus, we propose that (a) Cu is the favored NO_3^- adsorption site, (b) nitrate transformation takes place on Cu active sites, and (c) electron transfer between the support and the active layer (BCN → Cu) further enhances the NO_3RR activity. It is also worth noting that if some of the Pd used for surface activation were accessible for nitrate ions despite the full copper coverage and the lack of evidence of Pd in the XPS spectra in Fig. 6, strongly adsorbed active hydrogen can be formed on Pd surfaces. These [H_{ad}] species then can act as a reducing agent to promote the intermediate nitrite reduction towards ammonia. Similar enhancement was revealed in a Cu/Ru system, where Ru provided active hydrogen for the nitrite-to-ammonia step of the process.[52]

It is also known in the literature that the catalytic activity of Cu depends on the exposed crystal facets, morphology, surface functionalization, vacancies, and heterointerfaces, while it also changes with dispersion in the single site ↔ single atom ↔ nanocluster ↔ nanoparticle ↔ thin layer line.[53] There is a dynamic reversible transformation in Cu catalysts during NO_3RR, where oxidation and re-dispersion of Cu transform single-atom sites into clusters and eventually, particles. It was proven that higher Cu loading and more negative electrode potential enhance this process.[54] Similar *in situ* restructuring accompanied by changing Cu oxidation state during the reduction process was found in a Cu/nickel foam system, where Cu_2O was loaded onto the electrochemically deposited Cu islands under reaction conditions.[39] Although XPS and DFT results showed that the improved ammonia yield was the result of the presence of stable Cu(I) species in the latter system, our Cu_2O/BCN possessed only low NO_3RR activity as it can be seen in Fig. 7c.

Also, nitrate reduction activity varied with changing Cu coverage on the Ru/C substrate, where nitrate conversion increased with the increase in Cu coverage between 0 and 0.6 ML Cu, above which no further activity enhancement was seen. It was proposed that the enhancement comes from a synergistic effect of blocking HER sites on the Ru surface and accelerating nitrate-to-nitrite reduction rate, while the underlying Ru substrate likely changes the electronic structure of Cu on the top. The latter effect persisted even up to full surface coverage (1 ML Cu). UHV-XPS results on 1 ML Cu/Ru(0001) indicated a strong interaction between Ru and Cu along with a higher copper electron density compared to that of its bulk counterpart. Furthermore, an upshift in the Cu d-band center was evidenced in Rh-supported 1 ML Cu by DFT calculations, which led to stronger N-containing intermediate adsorption. As a result, both nitrite adsorption, and nitrite reduction were facilitated on Cu/Ru due to the beneficial electronic coupling.[52] Although similar effects are anticipated in other supported systems, BCN-supported NO_3RR catalysts are largely unexplored.

4. Conclusions

Boron–carbon–nitrogen ($B_xC_yN_z$) was successfully synthesized through a newly developed hybrid approach. The combination of mechanical alloying and subsequent calcination (pyrolysis) resulted in an amorphous and porous BCN structure. By increasing the annealing temperature, a higher-purity $B_xC_yN_z$ phase was obtained. Afterward, a thin copper layer was deposited on the as-synthesized $B_xC_yN_z$ *via* electroless plating with and without prior palladium surface activation. By applying Pd^{2+} activation, a pure copper layer was deposited onto the BCN particles, and a Cu@BCN core/shell composite was formed. On the other hand, the activation-less Cu plating resulted in an unevenly deposited Cu_2O-on-BCN structure. The obtained composites were tested in alkaline electrochemical nitrate reduction, and the Cu@BCN composites showed the highest NO_3RR activity compared to those of the as-synthesized BCN and the Cu_2O/BCN samples.

Conflicts of interest

The authors declare no competing interest.

Data availability

The data supporting this article have been included as part of the ESI.† Further data of the measurement results can be requested from the authors.

Acknowledgements

ATT acknowledges the financial support of the MTA Sustainable Development and Technologies National Programme of MTA, Sustainable Technologies Sub-Programme (NP2022-II-7/2022). HH acknowledges the financial support of the János Bolyai Research Grant of the Hungarian Academy of Sciences (BO/682/22). Project no. RRF-2.3.1-21-2022-00009 (National Laboratory for Renewable Energy) has been implemented with the support provided by the Recovery and Resilience Facility of the European Union within the framework of Programme Széchenyi Plan Plus. The project received funding from the HUN-REN Hungarian Research Network. ZK is grateful for K 21 138714 and SNN_135918 projects of the National Research, Development and Innovation Fund. TKP2021-NVA-19 under the TKP2021-NVA funding scheme of the Ministry for Innovation and Technology are acknowledged. RV acknowledges the MTA Distinguished Guest Scientist Fellowship Programme 2024 of the Hungarian Academy of Sciences (MTA).

References

1 S. D. Nehate, A. K. Saikumar, A. Prakash and K. B. Sundaram, *Mater. Today Adv.*, 2020, **8**, 100106.
2 A. Ranjbar Aghjehkohal, A. Taghizadeh Tabrizi and M. Yildiz, *J. Alloys Compd.*, 2023, **962**, 171159.
3 R. Bahadur, G. Singh, Y. Bando and A. Vinu, *Carbon*, 2022, **190**, 142–169.
4 D. Kurapov, D. Neuschütz, R. Cremer, T. Pedersen, M. Wuttig, D. Dietrich, G. Marx and J. M. Schneider, *Vacuum*, 2002, **68**, 335–339.
5 T. Kida, K. Shigezumi, M. A. Mannan, M. Akiyama, Y. Baba and M. Nagano, *Vacuum*, 2009, **83**, 1143–1146.
6 Z. F. Ying, D. Yu, H. Ling, N. Xu, Y. F. Lu, J. Sun and J. D. Wu, *Diamond Relat. Mater.*, 2007, **16**, 1579–1585.
7 T. Zhang, J. Zhang, G. Wen, B. Zhong, L. Xia, X. Huang, H. Zhao, H. Wang and L. Qin, *Carbon*, 2018, **136**, 345–358.
8 S. Xu, A. Dong, Y. Hu, Z. Yang, S. Huang and J. Qian, *J. Mater. Chem. A*, 2023, **11**, 9721–9747.
9 X. Wang, A. Dong, Y. Hu, J. Qian and S. Huang, *Chem. Commun.*, 2020, **56**, 10809–10823.
10 J. A. Oke and T.-C. Jen, *J. Mater. Res. Technol.*, 2022, **21**, 2481–2514.

11 E. A. Malinina, I. I. Myshletsov, G. A. Buzanov, I. V. Kozerozhets, N. P. Simonenko, T. L. Simonenko, S. E. Nikiforova, V. V. Avdeeva, K. Y. Zhizhin and N. T. Kuznetsov, *Inorganics*, 2023, **11**, 345.
12 T. Balakrishnan, K. U. V. Kiran, S. M. Kumar, A. Raju, S. A. Kumar and S. Mayavan, *J. Environ. Chem. Eng.*, 2017, **5**, 564–571.
13 S. Kalimuthu, I. Meenakshisundaram, G. Ponnaiah and K. Sekar, *Mater. Chem. Phys.*, 2018, **219**, 204–211.
14 R. Melentiev, A. Yudhanto, R. Tao, T. Vuchkov and G. Lubineau, *Mater. Des.*, 2022, **221**, 110958.
15 IEA, *Ammonia Technology Roadmap*, IEA, Paris, 2021, **https://www.iea.org/reports/ammonia-technology-roadmap**, Licence: CC BY 4.0.
16 H. Xu, Y. Ma, J. Chen, W.-X. Zhang and J. Yang, *Chem. Soc. Rev.*, 2022, **51**, 2710–2758.
17 Y. Zeng, C. Priest, G. Wang and G. Wu, *Small Methods*, 2020, **4**, 2000672.
18 T. Kokulnathan and T.-J. Wang, *Composites, Part B*, 2019, **174**, 106914.
19 X. Li, X. Zhao, Y. Zhou, J. Hu, H. Zhang, X. Hu and G. Hu, *Appl. Surf. Sci.*, 2022, **584**, 152556.
20 B. Xu, D. Li, Q. Zhao, S. Feng, X. Peng and P. K. Chu, *Coord. Chem. Rev.*, 2024, **502**, 215609.
21 L. Yang, J. Li, F. Du, J. Gao, H. Liu, S. Huang, H. Zhang, C. Li and C. Guo, *Electrochim. Acta*, 2022, **411**, 140095.
22 D. Jang, J. Maeng, J. Kim, H. Han, G. H. Park, J. Ha, D. Shin, Y. J. Hwang and W. B. Kim, *Appl. Surf. Sci.*, 2023, **610**, 155521.
23 Z. Shen, J. Yan, M. Wang, L. Xing, B. Huang, H. Zhou, W. Li, L. Chen and J. Shi, *ACS Sustainable Chem. Eng.*, 2023, **11**, 9433–9441.
24 L. Bai, F. Franco, J. Timoshenko, C. Rettenmaier, F. Scholten, H. S. Jeon, A. Yoon, M. Rüscher, A. Herzog, F. T. Haase, S. Kühl, S. W. Chee, A. Bergmann and R. C. Beatriz, *J. Am. Chem. Soc.*, 2024, **146**, 9665–9678.
25 X. Zhao, X. Jia, H. Zhang, X. Zhou, X. Chen, H. Wang, X. Hu, J. Xu, Y. Zhou, H. Zhang and G. Hu, *J. Hazard. Mater.*, 2022, **434**, 128909.
26 J. V. Perales-Rondon, D. Rojas, W. Gao and M. Pumera, *ACS Sustainable Chem. Eng.*, 2023, **11**, 6923–6931.
27 D. Chen, X. Hu, Y. Huang, Y. Qian and D. Li, *Mater. Lett.*, 2019, **246**, 28–31.
28 P. Wang, P. Wang, Y. Guo, L. Rao and C. Yan, *Chem. Eng. J.*, 2021, **412**, 128532.
29 M. Mirzaee, A. Rashidi, A. Zolriasatein and M. Rezaei Abadchi, *Diamond Relat. Mater.*, 2021, **115**, 108350.
30 P. Bhattacharyya, S. Sahoo, A. H. Seikh, S. M. A. K. Mohammed, A. Sarkar and N. Alharthi, *Diamond Relat. Mater.*, 2019, **92**, 235–241.
31 C. Gui, C. Yao, J. Huang, Z. Chen and G. Yang, *Appl. Surf. Sci.*, 2020, **506**, 144935.
32 Q. Zhang, L. Ning, C. Wang, M. Wang, Y. Shen and Y. Yan, *J. Mater. Sci.: Mater. Electron.*, 2019, **30**, 14631–14645.
33 C. Wang, L. Zeng, W. Ding and T. Liang, *Vacuum*, 2021, **191**, 110330.
34 L. Luo, P. Li, X. Liu, W. Zeng, Y. Zhang, M. Liu and S. Yao, *Electrochim. Acta*, 2023, **439**, 141679.
35 Y. Wei, P. Wu, J. Luo, L. Dai, H. Li, M. Zhang, L. Chen, L. Wang, W. Zhu and H. Li, *Microporous Mesoporous Mater.*, 2020, **293**, 109788.
36 J. Li, N. Lei, H. Hao and J. Zhou, *Chem. Phys. Lett.*, 2017, **672**, 99–104.
37 B. Alavi, H. Aghajani and A. Rasooli, *J. Eur. Ceram. Soc.*, 2019, **39**, 2526–2534.
38 B. Alavi, H. Aghajani and A. Rasooli, *Thin Solid Films*, 2019, **669**, 514–519.
39 C. Wang, F. Ye, J. Shen, K.-H. Xue, Y. Zhu and C. Li, *ACS Appl. Mater. Interfaces*, 2022, **14**, 6680–6688.
40 W. Liu, T. Yanase, T. Nagahama and T. Shimada, *J. Alloys Compd.*, 2019, **792**, 1206–1212.
41 M. Zhou, S. Li, S. Wang, Z. Jiang, C. Yang, F. Guo, X. Wang and W.-K. Ho, *Appl. Surf. Sci.*, 2022, **599**, 153985.
42 Y. Chen, P. Zhang, L. Jiao, G. Chen, Y. Yang, H. Chong and M. Lin, *Chem. Eng. J.*, 2022, **446**, 137337.
43 R. Betancourt-Galindo, P. Y. Reyes-Rodriguez, B. A. Puente-Urbina, C. A. Avila-Orta, O. S. Rodríguez-Fernández, G. Cadenas-Pliego, R. H. Lira-Saldivar and L. A. García-Cerda, *J. Nanomater.*, 2014, **2014**, 980545.
44 A. Prakash and K. B. Sundaram, *Diamond Relat. Mater.*, 2016, **64**, 80–88.
45 G. A. Cerrón-Calle, A. S. Fajardo, C. M. Sánchez-Sánchez and S. Garcia-Segura, *Appl. Catal., B*, 2022, **302**, 120844.
46 W. H. Lee, H. N. Yang, K. W. Park, B. S. Choi, S. C. Yi and W. J. Kim, *Energy*, 2016, **96**, 314–324.
47 J. M. McEnaney, S. J. Blair, A. C. Nielander, J. A. Schwalbe, D. M. Koshy, M. Cargnello and T. F. Jaramillo, *ACS Sustainable Chem. Eng.*, 2020, **8**, 2672–2681.
48 S. Z. Andersen, V. Čolić, S. Yang, J. A. Schwalbe, A. C. Nielander, J. M. McEnaney, K. Enemark-Rasmussen, J. G. Baker, A. R. Singh, B. A. Rohr, M. J. Statt, S. J. Blair, S. Mezzavilla, J. Kibsgaard, P. C. K. Vesborg, M. Cargnello, S. F. Bent, T. F. Jaramillo, I. E. L. Stephens, J. K. Nørskov and I. Chorkendorff, *Nature*, 2019, **570**, 504–508.
49 Z.-Y. Wu, M. Karamad, X. Yong, Q. Huang, D. A. Cullen, P. Zhu, C. Xia, Q. Xiao, M. Shakouri, F.-Y. Chen, J. Y. Kim, Y. Xia, K. Heck, Y. Hu, M. S. Wong, Q. Li, I. Gates, S. Siahrostami and H. Wang, *Nat. Commun.*, 2021, **12**, 2870.
50 X. Fu, X. Zhao, X. Hu, K. He, Y. Yu, T. Li, Q. Tu, X. Qian, Q. Yue, M. R. Wasielewski and Y. Kang, *Appl. Mater. Today*, 2020, **19**, 100620.
51 C. Wang, Z. Liu, L. Dong, F. Du, J. Li, C. Chen, R. Ma, C. Li and C. Guo, *J. Power Sources*, 2023, **556**, 232523.
52 J.-Q. Chen, X.-X. Ye, D. Zhou and Y.-X. Chen, *J. Phys. Chem. C*, 2023, **127**, 2918–2928.
53 R. Zhang, S. Zhang, H. Cui, Y. Guo, N. Li and C. Zhi, *Next Energy*, 2024, **4**, 100125.
54 X.-Y. Ji, K. Sun, Z.-K. Liu, X. Liu, W. Dong, X. Zuo, R. Shao and J. Tao, *Nano-Micro Lett.*, 2023, **15**, 110.